



Simultaneous Twinning and Microband-Induced Plasticity of a Compositionally Complex Alloy with Interstitial Carbon at Cryogenic Temperatures

A. S. Tirunilai¹ · R. Osmundsen² · I. Baker² · H. Chen^{3,4} · K.-P. Weiss³ · M. Heilmaier¹ · A. Kauffmann¹

Received: 7 March 2022 / Accepted: 29 April 2022
© The Author(s) 2022

Abstract

Intermediate to low stacking fault energy (SFE) high entropy alloys (HEA) have shown an excellent combination of strength and ductility as a result of deformation twinning and martensite transformation. However, even in the absence of these mechanisms HEA can show a good strength-ductility combination, as is the case with non-equiatomically (Fe_{40.4}Ni_{11.3}Mn_{34.8}Al_{7.5}Cr₆)C_{1.1}. The room temperature mechanical behavior of this alloy has been associated with Taylor lattice and microband formation. The current research focuses on tensile cryogenic deformation of this alloy and investigates if these features and/or alternate mechanisms like deformation twinning are obtained. Surprisingly, it is not one or the other but both deformation twinning and microband formation that are observed during cryogenic deformation. The activation of both deformation mechanisms is a combination that is not often reported as the former is generally associated with intermediate to low SFE alloys and the latter with intermediate to high SFE alloys. The activation of twinning in (Fe_{40.4}Ni_{11.3}Mn_{34.8}Al_{7.5}Cr₆)C_{1.1} is attributed to the high yield stress-temperature variation, as a result of solid solution strengthening being far greater than in other commonly researched compositionally complex alloys. A ductility retention down to 4 K was observed, while simultaneously showing a significant increase in flow stress. Despite the intermediate to high SFE deformation behavior, (Fe_{40.4}Ni_{11.3}Mn_{34.8}Al_{7.5}Cr₆)C_{1.1} exhibits excellent cryogenic strength-ductility combination.

Keywords Twinning · Microbands · HEA · Interstitial solid solution

Introduction

High-entropy alloys (HEA) are a class of alloys that have garnered significant attention in the recent past [1–7]. They consist of multiple principal elements as opposed to conventional alloys consisting of single principal element [3]. The bulk of the formerly carried out research has been focused

on equiatomically face-centered cubic (FCC) [8, 9] and body-centered cubic (BCC) [10, 11] alloys. While these alloys have a potential in certain applications, for example biocompatible materials [12], they are most often considered for their excellent mechanical properties [13]. Among FCC alloys a significant focus has been placed on equiatomically alloys from the Co–Cr–Fe–Mn–Ni system [9, 14, 15]. These alloys have shown an excellent strength–ductility retention down to 4 K [14, 16–18] which has been attributed to the activation of deformation twinning [19], as a result of their low stacking fault energy (SFE) (< 35 mJ m⁻² [20]). Some alloys such as CoCrNi, additionally show martensite transformation at cryogenic temperatures [17, 21], characteristic of even lower SFE (< 18 mJ m⁻² [20]). Li et al. [22, 23] were able to synthesize a series of high-Mn alloys, wherein the SFE is low enough to show martensite transformation during room temperature deformation itself.

While the above-mentioned alloys have shown that activation of twinning or martensite transformation during deformation are effective work-hardening mechanisms, they aren't

✉ A. Kauffmann
alexander.kauffmann@kit.edu

¹ Institute for Applied Materials (IAM-WK), Karlsruhe Institute of Technology (KIT), Engelbert-Arnold-Str. 4, 76131 Karlsruhe, Germany

² Thayer School of Engineering, Dartmouth College, Hanover, NH 03755, USA

³ Institute for Technical Physics (ITEP), Karlsruhe Institute of Technology (KIT), Hermann-von-Helmholtz-Platz 1, 76344 Eggenstein-Leopoldshafen, Germany

⁴ Present Address: Vacuumschmelze GmbH & Co. KG, Grüner Weg 37, 63450 Hanau, Germany

the only way to achieve high work-hardening rates. Even in the absence of these mechanisms, HEA may show excellent strength–ductility combination, as is the case with non-equiatomic FCC $\text{Fe}_{40.4}\text{Ni}_{11.3}\text{Mn}_{34.8}\text{Al}_{7.5}\text{Cr}_6$, doped with a nominal content of 1.1 at.% C. This alloy has formerly been tested at RT and reported as having excellent strength, as a result of solid solution strengthening from interstitial C [24]. The microstructural features in $(\text{Fe}_{40.4}\text{Ni}_{11.3}\text{Mn}_{34.8}\text{Al}_{7.5}\text{Cr}_6)\text{C}_{1.1}$ include the formation of Taylor lattices as well as microbands [24]. Microbands have been observed during tensile deformation at temperatures as high as 673 K in this alloy [25] and have been reported as increasing the work-hardening rate [26]. These features are more often reported in intermediate to high-SFE materials ($> 35 \text{ mJ m}^{-2}$ [20]) [26, 27].

While room and high-temperature deformation characteristics are clear, tensile deformation at cryogenic temperatures has not been as intensely investigated. It is not apparent if the Taylor lattices and microbands will be generated at lower temperatures. This is questionable since decreasing temperatures correspond with decreasing SFE in several FCC alloy systems, including Cu-based alloys, Ni-based alloys, steels and multi-principle alloys [28–32]. Thus, these features may not be observed during cryogenic deformation. As a consequence, the work-hardening rate of the material might be affected and its strength/ductility at lower temperatures would be compromised. Alternatively, if the SFE decreases substantially, deformation twinning might instead be activated, which would contribute positively to work hardening and ductility.

Based on this, the following scientific questions become relevant: (i) Would microband formation extend to lower temperatures, despite the expected decrease in SFE? (ii) Would twinning be activated at these lower temperatures? (iii) Does the interstitial C play a role in this? (iv) What are the contributions of these mechanisms to work hardening?

The present article thus focuses on tensile deformation in $(\text{Fe}_{40.4}\text{Ni}_{11.3}\text{Mn}_{34.8}\text{Al}_{7.5}\text{Cr}_6)\text{C}_{1.1}$ at cryogenic temperatures down to 4 K, with the goal of understanding transition in deformation behavior with decreasing temperature.

Experimental Procedure

Alloy Synthesis

The alloy $(\text{Fe}_{40.4}\text{Ni}_{11.3}\text{Mn}_{34.8}\text{Al}_{7.5}\text{Cr}_6)\text{C}_{1.1}$ was synthesized from elemental pieces of Fe (99.8%), Ni (99.95%), Mn (99.8%), Al (99.8%), Cr (99%) and Fe_3C (99.8%) melted in the appropriate ratios. The elements were arc-melted in a water-chilled Cu crucible, in an Ar atmosphere. Tensile specimens were machined from the cast. These specimens were then homogenized in an evacuated glass ampule at 1423 K for 8 h and quenched in water. The homogenized

samples were ground and then polished with 3 and 1 μm diamond suspensions followed by an oxide polishing suspension (OP-S) of pH 9.8, supplied by Struers.

Materials Characterization

Microstructural investigations and X-ray diffraction analyses were carried out after a standard metallographic preparation of the specimens. The specimens were first ground with a series of abrasive SiC papers of increasing grit number; they were then polished using 3 and 1 μm diamond suspensions. This was followed by a non-crystallizing oxide polishing suspension (OP-S) with a pH 9.8, supplied by Struers, as described above. XRD was carried out with a Cu-K α radiation over the 2Θ range 10° – 145° using a D2 Phaser system by Bruker equipped with a LynxEye line detector. The lattice parameter was determined by extrapolation with $\frac{1}{2} \cdot (\cot^2\Theta + \cot\Theta \cdot \cos\Theta)$ to $\Theta = 90^\circ$ similar to the Nelson–Riley approach [33]. Backscattered electron (BSE) and secondary electron (SE) imaging was performed using an Apreo scanning electron microscope (SEM; Thermo Fisher Scientific Inc.) utilizing a circular backscatter (CBS) detector as well as a Zeiss Evo 50 SEM. Electron backscatter diffraction (EBSD) was carried out on the deformed samples using the Apreo with a Pegasus EBSD system by EDAX. The EBSD results were evaluated using OIM Analysis software by EDAX. Energy dispersive X-ray spectroscopy (EDX) was carried out in a Zeiss Evo 50 SEM using a Thermo Scientific EDX system to the concentrations of the metallic components, specifically to ensure that Mn losses were not excessive. The deviations were found to be less than 1.5 at.%, with no Mn loss detected.

Samples deformed to fracture were additionally investigated by transmission electron microscopy (TEM). Disks of 3 mm diameter were produced from the uniform deformation regions by electro-discharge machining and then ground to $<100 \mu\text{m}$ thickness. These specimens were electropolished in an electrolyte of 15% nitric acid and 85% methanol using a Struers Tenupol 5 twin-jet electropolisher at 12.5 V, $\sim 50 \text{ mA}$ and $\sim 250 \text{ K}$. The electropolished thin foils were washed in methanol and ethanol alternately three times and then rinsed in methanol. The TEM investigations were carried out using an FEI Tecnai F20 FEG TEM operated at 200 kV.

Mechanical Testing

Tensile tests were carried out at 295 K (room temperature), 77 K (submerged in liquid Nitrogen) and 4 K (submerged in liquid Helium). These tests were performed at the Cryogenic Material Test Lab Karlsruhe (CryoMaK, KIT), an account of the process is given in Ref. [34]. The cylindrical tensile specimens have M6 connecting threads, a total length of 45 mm, a gauge length of 22 mm, transition radii of

10 mm, and a gauge diameter of 4 mm. Tensile testing was performed until fracture with constant crosshead movement of 0.5 mm min^{-1} , corresponding to an initial plastic strain rate of $3 \times 10^{-4} \text{ s}^{-1}$, under standard conditions according to ASTM E8M [35]. The specimen elongation was measured using two clip-on extensometers attached to the gauge section (clip-on extensometers setup requires an even number of extensometers). Force, elongation and time data were used to derive stress-, strain-, work-hardening rates as well as other parameters, using the proprietary software package Origin 2019 by OriginLab. At 4 K, a severely discontinuous deformation was observed. The local stress maxima and associated parameters of these discontinuities were identified using a script, written by the authors in MATLAB R2018a (MathWorks). For a detailed explanation on the data identification and handling procedure for discontinuous deformation, please refer to Ref. [16].

Results and Discussion

Yield Stress-Temperature Variation

Figure 1a illustrates the XRD pattern post-homogenization confirming that no additional carbides were formed during the heat treatment. Figure 1b also shows the initial microstructure at this point. The grains are several hundred microns in diameter, similar to the as-cast microstructure investigated in Ref. [24].

Tensile tests were carried out at an extension rate corresponding to an initial strain rate of $3 \cdot 10^{-4} \text{ s}^{-1}$ on the specimens at RT, 77 K and 4 K. The yield stress (σ_{YS}) dependence on temperature is as depicted in Fig. 2a. Data for pure Ni

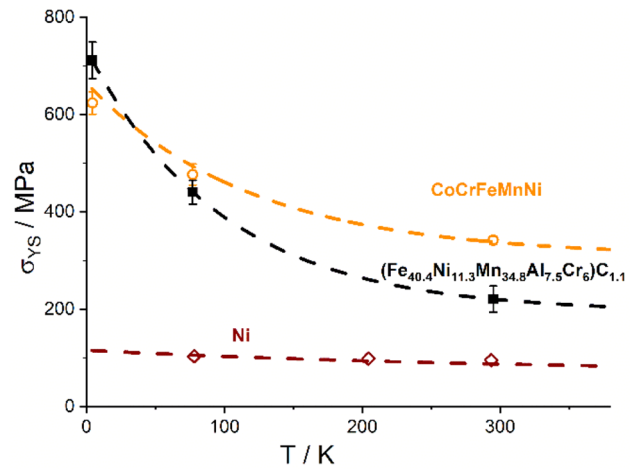


Fig. 2 Plot of $\sigma_{YS} - T$ for CoCrFeMnNi, $(\text{Fe}_{40.4}\text{Ni}_{11.3}\text{Mn}_{34.8}\text{Al}_{7.5}\text{Cr}_6)\text{C}_{1.1}$ and Ni [9, 14, 17]

and equiatomic CoCrFeMnNi are included for comparison [9, 14, 17].

All three FCC metals/alloys increase in strength as the temperature decreases, as is expected. The variation of σ_{YS} , based on temperature is primarily attributed to the variation in Peierls–Nabarro (PN) stress, which in turn is thermally assisted at ambient temperatures [36]. This thermal assistance decreases as the temperature approaches absolute zero.

For solid solutions the PN stress consists of both lattice friction and solute contributions through lattice distortion. Thus, the lack of thermal assistance affects solid solutions more prominently. This is clear from the steep change in $\sigma_{YS} - T$ for the HEAs in comparison to unalloyed Ni (Fig. 2a). The lines fitted to the data points were of the form given in Ref. [9]:

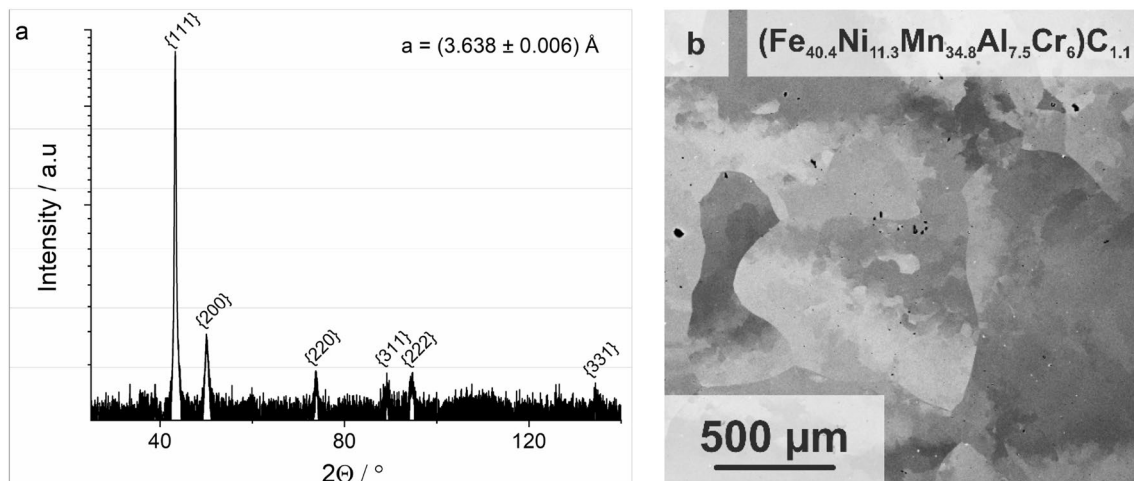


Fig. 1 **a** XRD pattern of $(\text{Fe}_{40.4}\text{Ni}_{11.3}\text{Mn}_{34.8}\text{Al}_{7.5}\text{Cr}_6)\text{C}_{1.1}$, after homogenization at 1150 °C for 8 h. Intensity is presented on a square root scale to clearly identify all peaks. **b** BSE image of the homogenized specimen

$$\sigma_{YS} = \sigma_{\text{thermal}} \cdot \exp\left(-\frac{T}{C}\right) + \sigma_{\text{athermal}} \quad (1)$$

Here σ_{thermal} and σ_{athermal} represent the temperature-dependent and -independent contributions to PN stress, respectively, T represents the temperature, and C is a fitting constant. The derivative of Eq. 1 with respect to temperature then becomes:

$$\frac{d\sigma_{YS}}{dT} = \sigma_{\text{thermal}} \cdot \left(-\frac{1}{C}\right) \cdot \exp\left(-\frac{T}{C}\right) \quad (2)$$

This may be simplified as:

$$\frac{d\sigma_{YS}}{dT} = -K_{\text{const}} \cdot \exp\left(-\frac{T}{C}\right), \text{ with } \left.\frac{d\sigma_{YS}}{dT}\right|_{T=0K} = -K_{\text{const}} \quad (3)$$

Here, K_{const} is the absolute value of the temperature-dependent derivative of $\sigma_{YS} - T$ at 0 K. A greater K_{const} implies a greater $\sigma_{YS} - T$ variation and correspondingly, a greater solid solution strengthening effect. Estimating solid solution strengthening is not straightforward in HEA, in the way that it is in binary alloys. In HEA, the lattice distortion may be estimated by root mean square atomic distance (MSAD^{0.5}) [37], where MSAD^{0.5} is the root mean square of the distance by which atoms in a lattice are displaced from their ideal distortion-free position, due to atomic size difference between solute and solvent atoms. Table 1 lists a series of equiatomic alloys from the Co–Cr–Fe–Mn–Ni system with the corresponding MSAD^{0.5} [37] and K_{const} values (K_{const} calculated from data in Ref. [9]). MSAD^{0.5} and K_{const} exhibit a linear variance with mild deviation, K_{const} being in the range of $\sim 1.2 - 2.4$. However, the K_{const} of 5.51 for (Fe_{40.4}Ni_{11.3}Mn_{34.8}Al_{7.5}Cr₆)C_{1.1} far exceeds the calculated values for these alloys, implying a significantly greater solid solution strengthening effect.

The much higher K_{const} can be attributed to interstitial C as opposed to substitutional solute contribution for alloys of the Co–Cr–Fe–Mn–Ni system. σ_{YS} at 4 K is ~ 3.2 times

that at RT for the present alloy, which far surpasses the ~ 1.8 times seen in equiatomic CoCrFeMnNi. Thus, even among concentrated solid solutions of high strength the solid solution strengthening effect in (Fe_{40.4}Ni_{11.3}Mn_{34.8}Al_{7.5}Cr₆)C_{1.1} is significantly higher.

It should be noted that one may consider the influence of other strengthening mechanisms to have a varied contribution with decreasing temperature, including orientation strengthening, Hall–Petch strengthening and dislocation strengthening. Particle strengthening may be disregarded since the alloy in question is a single-phase FCC alloy. Orientation and dislocation strengthening do not vary since the initial specimen preparation is the same and σ_{YS} was determined from three tests for each temperature, indicating consistency of values. Hall–Petch constant is expected to increase with decreasing temperature, but is responsible only for minor contribution $< 0.1 \cdot \sigma_{\text{CRSS}}$ (σ_{CRSS} is critical resolved shear stress) [17], which is far less than the factor of change of ~ 3.2 , for the yield strength at room temperature vs. at 4 K presently observed. In accordance with this the rate of change of $\sigma_{YS} - T$ was attributed to primarily solid solution strengthening.

Tensile Deformation Behavior

The engineering stress–strain ($\sigma_e - \epsilon_e$) curves are displayed in Fig. 3 along with their corresponding true work-hardening plots. As stated in the previous section it is clear to see that σ_{YS} and ultimate tensile strength (σ_{UTS}) increase with decreasing temperature. However, the elongation is not compromised, approaching an engineering strain (ϵ_e) around 40% even at 4 K. The fracture surfaces appear similar in all three cases showing dimple fracture (Fig. 4). The scale of the features becomes finer with decreasing temperature, but it clearly remains dimple fracture.

More interestingly, the work-hardening plots depict much greater initial work-hardening rates at cryogenic temperatures (Fig. 3b). This greater work-hardening rate is likely owed to different deformation mechanisms at RT in comparison to cryogenic temperatures. Work-hardening rates are plotted against true strain in the current case. True stress was avoided as comparability would be lost by the vastly different σ_{YS} . Deformation at 4 K is discontinuous/serrated in nature. Work-hardening trends for this case were determined using serration maxima which refer to the local stress peaks prior to each stress drop as seen at 4 K in Fig. 3a. All three curves are processed by interpolation and smoothening, but owing to the difference in point to point separation at 4 K, in comparison to the smooth deformation seen at 77 K and RT, the final result appears different.

Discontinuous or serrated plastic deformation observed for (Fe_{40.4}Ni_{11.3}Mn_{34.8}Al_{7.5}Cr₆)C_{1.1} has been reported

Table 1 List of alloys from the Co–Cr–Fe–Mn–Ni system, corresponding MSAD^{0.5} [37] and K_{const} (calculated from data in Ref. [9])

Alloy	MSAD ^{0.5} (pm)	K_{const} (MPa K ⁻¹)
CrMnFeCoNi	5.02	2.35
MnFeCoNi	4.08	1.29
CrFeCoNi	5.46	2.41
CrMnCoNi	6.37	2.37
CrCoNi	5.25	2.14
MnFeNi	4.71	1.45
MnCoNi	4.68	1.59
FeCoNi	4.03	1.16

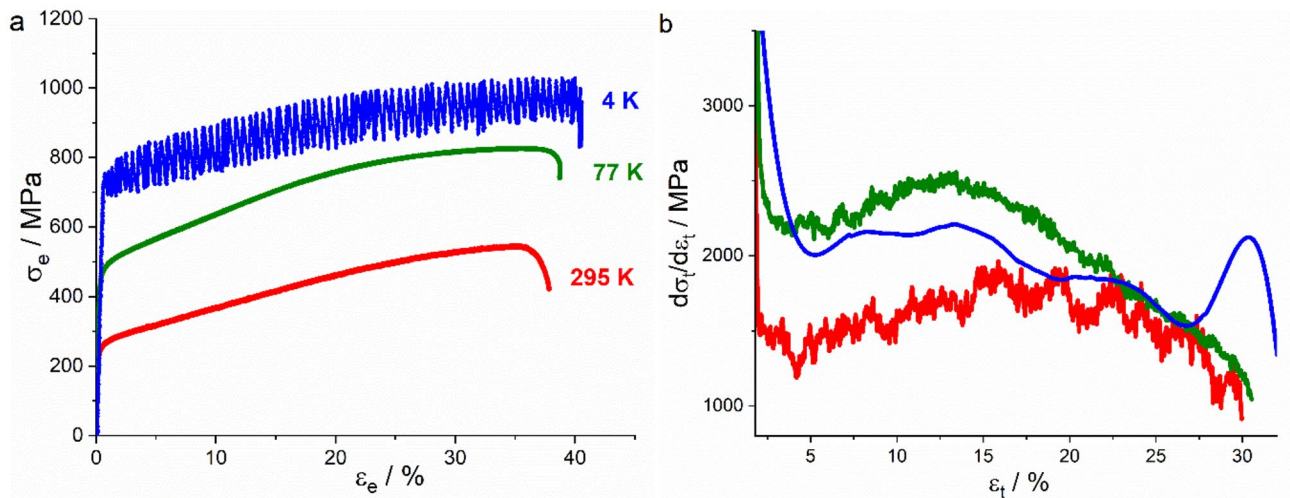


Fig. 3 **a** $\sigma_e - \epsilon_e$ plot for $(\text{Fe}_{40.4}\text{Ni}_{11.3}\text{Mn}_{34.8}\text{Al}_{7.5}\text{Cr}_6)\text{C}_{1.1}$ and corresponding **b** $\frac{d\sigma_t}{d\epsilon_t} - \epsilon_t$ plot. The data for all three plots in **b** have been smoothed. For 4 K in **(b)**, only maxima were considered

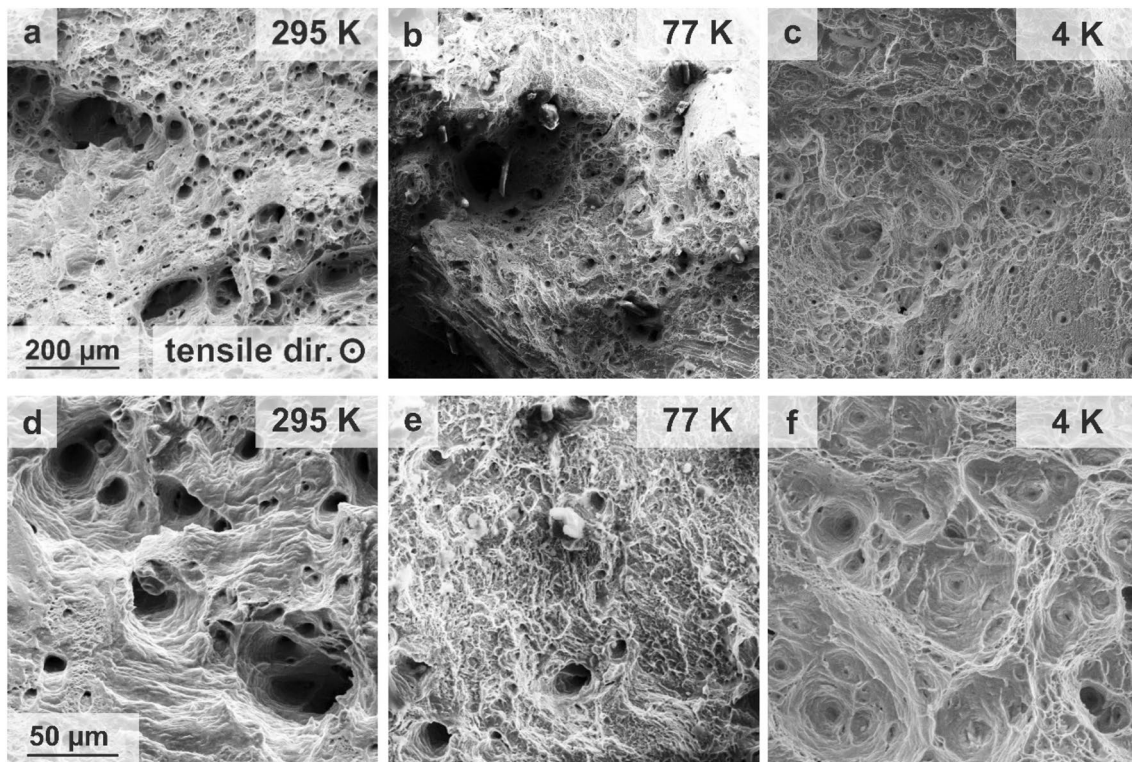


Fig. 4 SE micrographs of fracture surfaces of specimens deformed at **a** & **d** 295 K, **b** & **e** 77 K and **c** & **f** 4 K. The scaling of **a-c** and **d-f** are the same

during deformation close to 0 K, for many different alloys [38–40], including HEAs [14, 16, 41, 42]. The origin of the serrations is related to activation of dislocation sources at dislocation pile ups, causing sudden localized strain and a corresponding stress drop [16, 43, 44]. A

more detailed account explaining the phenomenological model, as observed for a single-phase FCC HEA, may be found in Ref. [16]. The stress drops observed currently, are ~ 50 – 150 MPa, in the same range as equiatomic CoCrFeMnNi [16]. Considering that the observations are in line

with other single-phase FCC alloys and serrated plastic deformation is not the focus of the present study it is not discussed in more detail. However, it should be noted that it has clearly been established that neither twinning nor transformation induced plasticity are linked to its cause [16, 39], so serrated plastic deformation does not validate or negate the activation of any deformation mechanism.

BSE micrographs depict partially deformed microstructures at $\epsilon_t \sim 10\%$ in Fig. 5, indicative of dislocation based deformation. While dislocation activity is expected and observed at all three temperatures, at both 77 and 4 K, additional long lenticular features are seen at high magnifications. These features were identified in Fig. 6 and were not found at RT even after deformation to fracture.

On the basis of subsequent EBSD (Fig. 7) and TEM analysis (Fig. 8d, e), these lenticular features were identified as deformation twins. Figure 7a, b, depict the post-fracture microstructure, with the bottom right representing an inverse pole figure (IPF) map and the top left representing an image quality (IQ) map. The IQ maps have $\Sigma 3$ twin boundaries marked in red. Correspondingly, deformation twins and twin boundaries are identified. It should be noted that while only a few distinct lamellae (indicated by the color change in IPF) are clearly obtained by EBSD, it is more likely that each of these ‘lamellae’ are actually twin bundles consisting of several nano-twins which are not distinctly indexed owing to the resolution limit of EBSD. These features are not intensely proliferated at earlier stages, but are easier to find at $\epsilon_t \sim 20\%$, as seen in Fig. 6c, d.

Figure 8d shows a TEM bright field (BF) image of the 77 K fractured sample with two deformation twins marked by red arrows. The spots in the corresponding SAD pattern effectively confirm that these are twins. The twins have a width in the range of 15–20 nm, similar to nano-twins reported in other FCC solid solutions [15, 19].

Stacking Fault Energy and Deformation Twinning

Deformation twinning is often seen in intermediate to low stacking fault energy (LSFE) ($< 35 \text{ mJ m}^{-2}$ [20]) materials [45–47]. The absence of deformation twinning during room temperature deformation of $(\text{Fe}_{40.4}\text{Ni}_{11.3}\text{Mn}_{34.8}\text{Al}_{7.5}\text{Cr}_6)\text{C}_{1.1}$ implies that the SFE is not sufficiently low to activate twinning, since the critical stress for twinning τ_{tw} may be considered to be directly proportional to SFE [48]. The following section highlights formation of microbands at RT, also indicative of intermediate to high SFE deformation ($> 35 \text{ mJ m}^{-2}$ [20]) [27, 49, 50].

Despite this, Wang et al. [24] have reported observing a wide stacking fault in the same alloy. The SFE calculated under specific assumptions was $\sim 10.2 \text{ mJ m}^{-2}$ [24]. However, it should be noted that this estimate was made from only two dislocations, both close to complete edge nature. When considering SFE determination by weak-beam TEM, multiple dislocations of different orientations are generally considered and appropriate SFE estimation is made considering an associated scatter [51]. Since the scatter shows a wide variation in SFE, as much as $\pm 9 \text{ mJ m}^{-2}$ for pure Cu [52], the estimations in Ref. [24] are likely not accurate enough. Apart from experimental error considered above, the wide SF maybe related two causes: (i) the Suzuki effect wherein the solute diffuses to the SF region and stabilizes the faulted region [53, 54]. Correspondingly, the SF would be stabilized and any weak beam investigations would lead to identifying wider SF as opposed to the intrinsic stacking fault width (SFW). (ii) Alternatively, solutes may interact with dissociated partial dislocations and affect the SFW [55, 56]. In both cases, the physically observed SFW may be varied localized segregations of solutes.

While atom probe tomography results have not clearly revealed segregation at nanometer scale [24], these segregations are expected to take place at an atomic level. Atomic scale segregations require even more intensive investigations, which is outside the present scope.

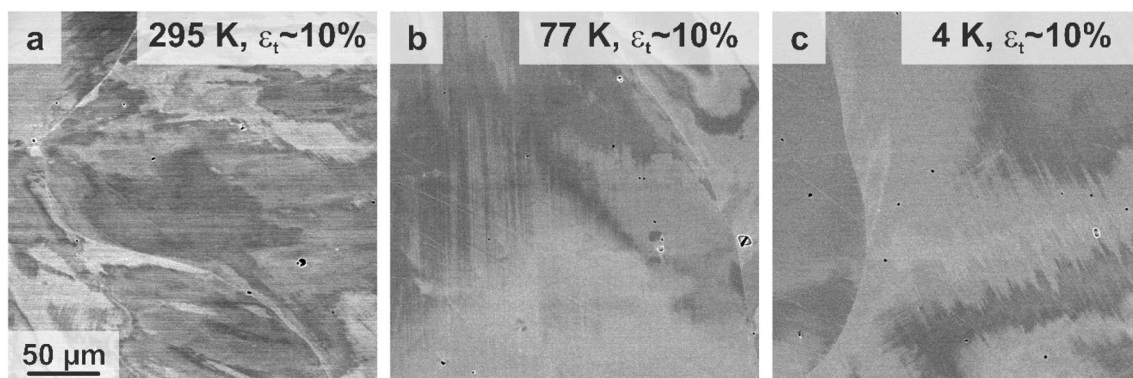


Fig. 5 BSE micrographs of specimens deformed to $\epsilon_t \sim 10\%$ at **a** 295 K, **b** 77 K and **c** 4 K

Fig. 6 BSE images of specimens deformed to $\epsilon_t \sim 10\%$ at **a** 77 K and **b** 4 K. BSE images of specimens deformed to $\epsilon_t \sim 20\%$ at **c** 77 K and **d** 4 K. Some long and lenticular features are marked by red arrows, these features are addressed below. The image scale is the same for all four images

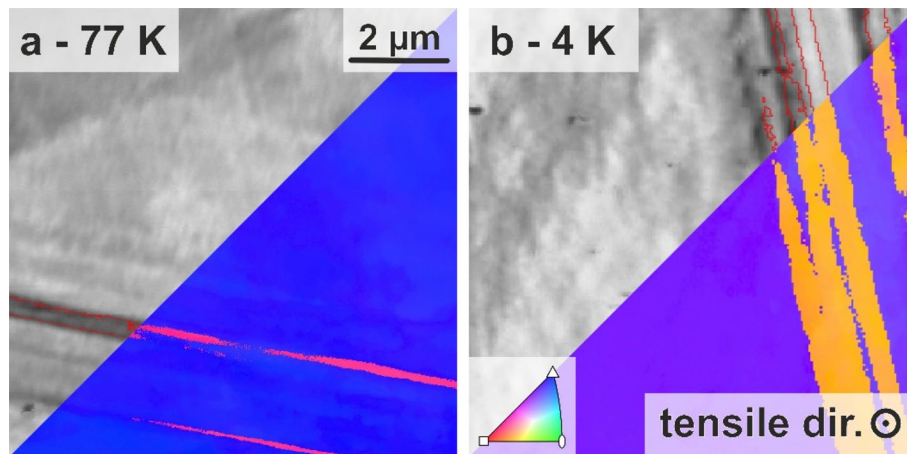
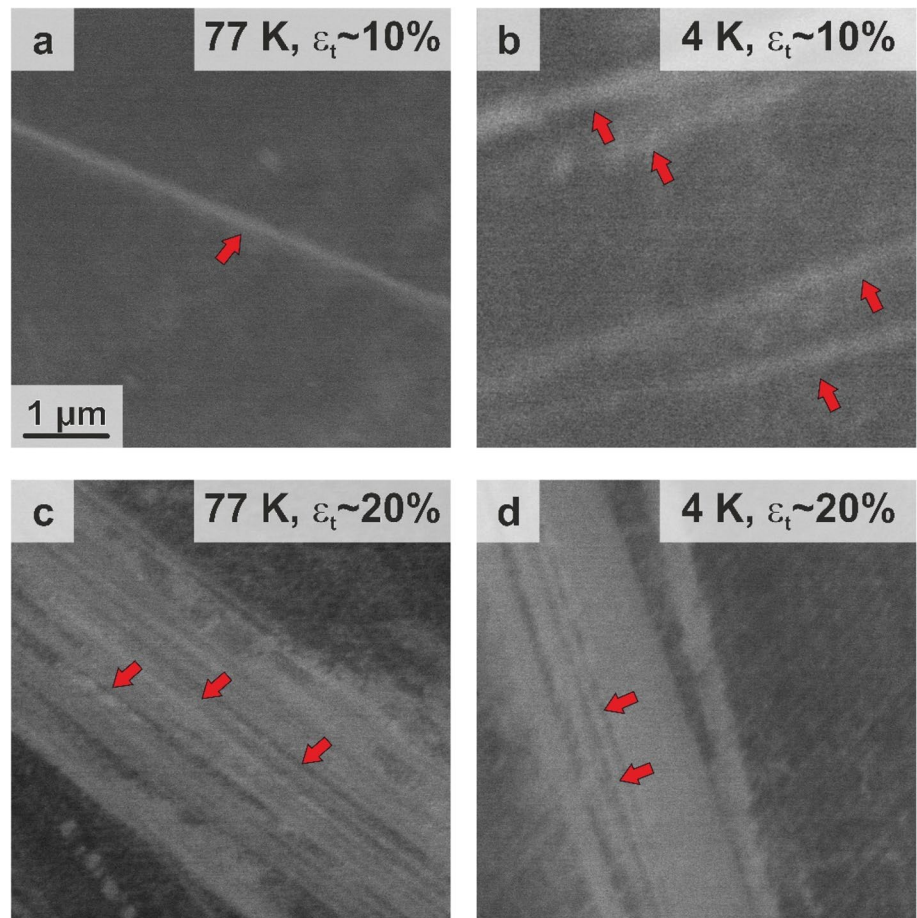


Fig. 7 EBSD maps for fractured samples tested at **a** 77 K and **b** 4 K. The top left half of the image is represented as an image quality (IQ) map and the bottom right half is represented as an inverse pole figure (IPF) map. The IPF legend for the tensile direction is as seen in the lower left corner of **b** and $\Sigma 3$ boundaries are indicated by red lines

in the IQ map. The image scale is the same for both images and both scans have been carried out on the sample cross section perpendicular to the tensile direction. (For interpretation of the references to color in this figure legend, the reader is referred to the web version of this article.)

Nevertheless, based on the above-presented ideas, the SFE evaluated in Ref. [24] is likely an underestimation. The experimentally determined SFW d_{exp} in Ref. [24] should have two contributions.

$$d_{\text{exp}} = d_{\text{int}} \pm d_{\text{sol}}$$

Here, d_{int} refers to the intrinsic SFW assuming no solute distortion/diffusion and d_{sol} is the offset acquired due to solute dislocation interaction. Depending on the local arrangement of atoms the distribution of solute atoms may either pin the trailing or leading dislocation more significantly than the other one, thus giving rise a wider or narrower SFW, respectively. This concept has been theoretically evaluated for solid solutions and validated with atomistic and dislocation dynamics simulations [57]. Given the circumstances, it may not be possible to easily estimate the intrinsic SFW devoid of solute influence but qualitative estimations of SFE may be made based on mechanical behavior.

To begin, as stated above, and validated by the microstructures shown here and in Refs. [24, 25, 58], the deformation behavior is that of an intermediate to high SFE material. Considering, that FCC alloy systems like Cu alloys, austenitic steels, Co–Ni, Co–Cr–Ni, Fe–Cr–Ni, Co–Fe, Fe–Mn–Cr–C systems [29, 30, 59], all show decreasing SFE with temperature, the alloy is expected to show different deformation behavior at lower temperatures. $(\text{Fe}_{40.4}\text{Ni}_{11.3}\text{Mn}_{34.8}\text{Al}_{7.5}\text{Cr}_6)\text{C}_{1.1}$ follows this trend, having an intermediate to high SFE at RT which decreases at cryogenic temperatures, validated by the absence or activation of twinning at respective temperatures.

Deformation twinning is activated in an alloy when a minimum stress, referred to as τ_{tw} is achieved, where τ_{tw} varies directly with SFE [48]. Correspondingly, as temperature decreases, τ_{tw} may be achieved due to the possible decrease in SFE. It is alternatively possible that the SFE variation plateaus at lower cryogenic temperatures, as seen in other alloys [29, 59]. Nevertheless, the increase in flow stress with decreasing temperature is significant for $(\text{Fe}_{40.4}\text{Ni}_{11.3}\text{Mn}_{34.8}\text{Al}_{7.5}\text{Cr}_6)\text{C}_{1.1}$ and thus, τ_{tw} is easily achieved at low temperatures regardless of whether SFE-T variation is mild or intense.

It should be noted that twin nucleation is associated with overcoming multiple energy barriers and associated parameters [60]. Apart from SFE, these include unstable SFE, twin stacking fault energy (TFE), and unstable TFE. These parameters are useful in estimating the energy changes associated with twin nucleation at atomic level [59, 60]. However, experimental estimates for these parameters are difficult and ab-initio calculations also require simplification [59, 60]. Byun [48] correlated experimentally determined twin stress to SFE showing reasonable consistency. Owing

to the lack of experimental data related to other parameters and the present study being restricted to a single alloy composition as well as considering macroscopic τ_{tw} of a polycrystalline specimen, τ_{tw} correlations are restricted to SFE for the present case. A quantitative analysis related to τ_{tw} in different compositions necessitates the consideration of twin formation energy pathways and all associated energy barriers. This is out of the scope of the present study and therefore neglected.

Post twin nucleation, deformation twins act as barriers to dislocations and strengthen the material through the dynamic Hall–Petch effect [15, 19]. This results in an additional work hardening, and since deformation twins are already observed at $\epsilon_t \leq 10\%$, the effects may be prominent at low strain. Correspondingly, at cryogenic temperatures, the work-hardening rate reaches a maximum of 2.2 – 2.5 GPa compared to 1.9 GPa at RT. Additionally, at cryogenic temperatures the work-hardening rate is in excess of 1.9 GPa for $\epsilon_t \leq 20\%$, implying the cumulative effect of work-hardening is even greater than what is gauged from just the maximum. While dislocation–dislocation interactions should lead to greater work-hardening at lower temperatures, they would scale with modulus values of the material. The elastic modulus changes only mildly from 147 GPa at RT to 159 GPa at 77 K, whereas the initial work-hardening rates increase from 1.3 to 2.2 GPa for the corresponding temperatures. This drastic jump necessitates an additional deformation mechanism. Thus, deformation twinning, that is operative at cryogenic temperatures, contributes positively to the work-hardening rate.

Dislocation Arrays and Microband Induced Plasticity

It is possible that microbands assist in work hardening at later stages of deformation [24], as opposed to early stage deformation with deformation twins [17, 19]. TEM investigations of the fractured samples revealed that the dislocation structures were different at RT and cryogenic temperatures (refer to Fig. 8). At RT, dislocations exist primarily in tangles. There are some indications of alignment of dislocation arrays, but they are not as strong. In contrast, at both 77 and 4 K, dislocations are arranged in well-defined linear intersecting arrays. The strong contrast variation at these arrays is because they are dense dislocation walls [27, 49, 50]. These features align themselves along the trace of $\{111\}$ planes within a tolerance of $\pm 5^\circ$. It should be noted, the progression of microstructure takes the form of dislocation tangles at low strains, domain boundaries defined by dislocation walls at higher strains followed by domain boundaries and microbands defined by dense dislocation walls at even greater strain [27, 50]. These features are not strictly sequential and overlap significantly, however, microbands and dense dislocation walls are far less common at lower strains.

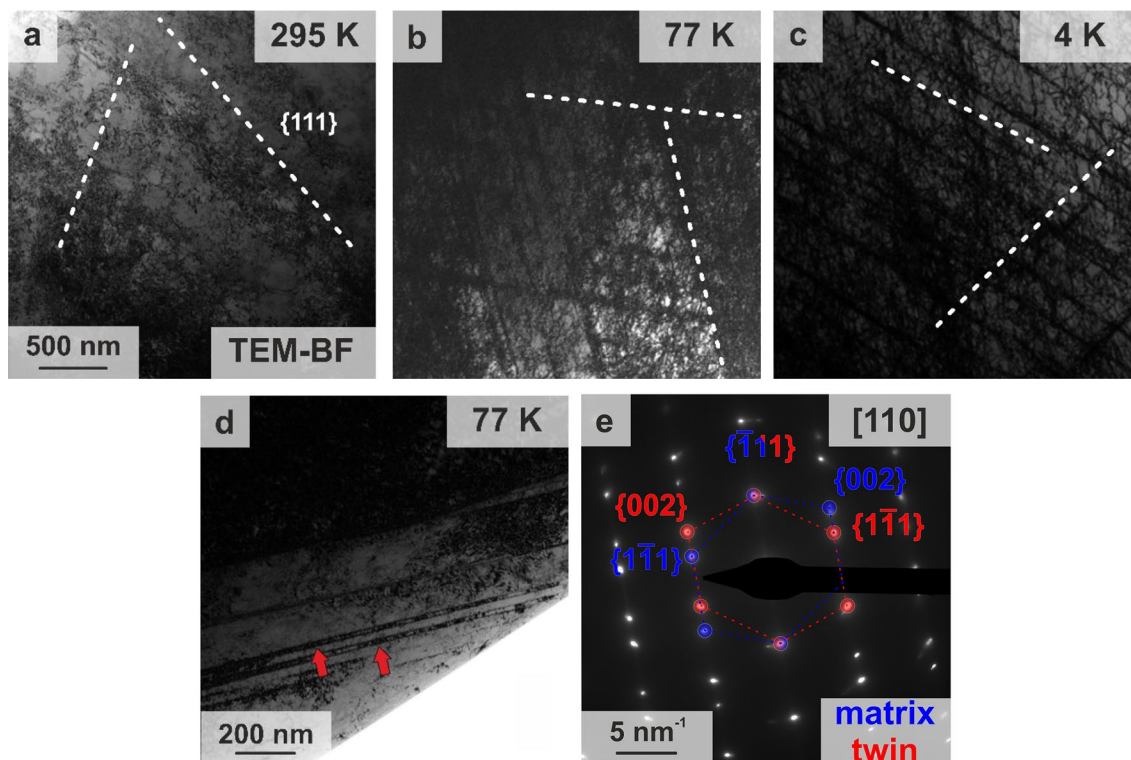


Fig. 8 TEM-BF images of fractured specimens deformed at **a** 295 K, **b** 77 K and **c** 4 K. The white dashed lines indicate traces of planes in the $\{111\}$ family. **d** TEM-BF image of specimen deformed at 77 K with twins marked by red arrows and corresponding **e** SAD pattern. The zone axis for the SAD pattern is $[110]$. SAD spots corresponding matrix and twin are marked in blue and red, respectively. The beam

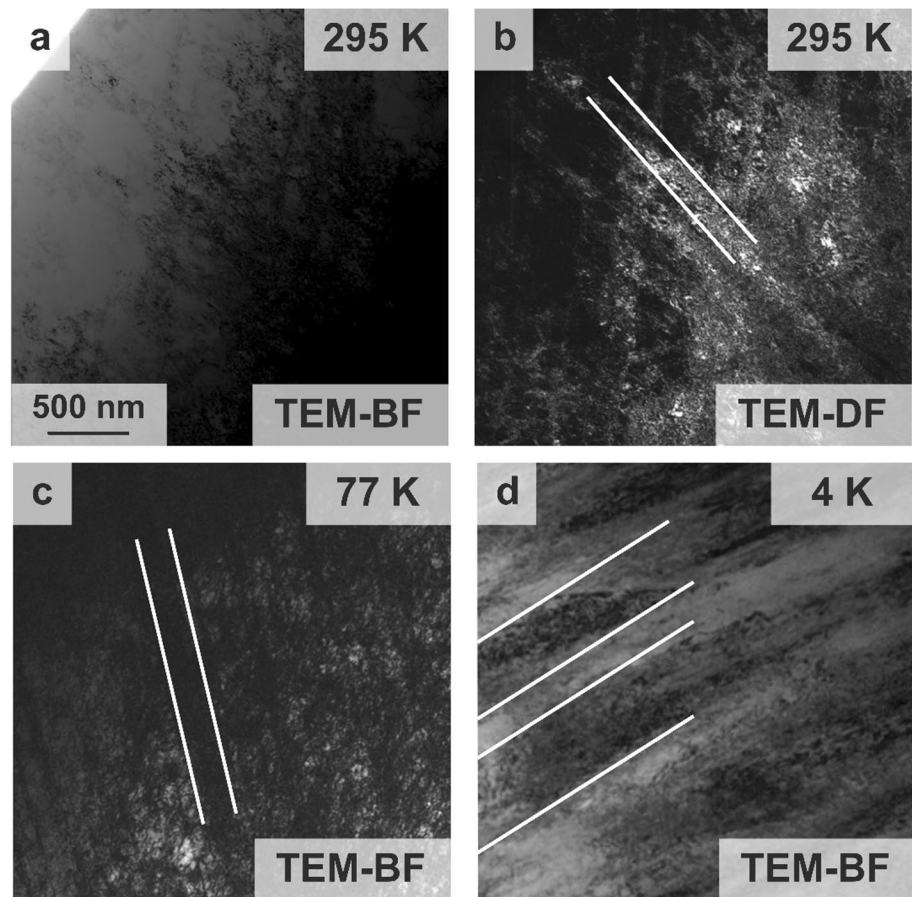
direction, \vec{B} , and diffraction vector, \vec{g} , used for each image are: **a** $\vec{B} = [110]$, $\vec{g} = [\bar{1}11]$; **b** $\vec{B} = [110]$, $\vec{g} = [\bar{1}11]$; **c** $\vec{B} = [111]$, $\vec{g} = [\bar{2}02]$; **d** $\vec{B} = [110]$, $\vec{g} = [\bar{1}11]$. (For interpretation of the references to color in this figure legend, the reader is referred to the web version of this article)

This raises the question of why the microstructure was at different stages of development at RT, 77 K and 4 K, if all the specimens failed at $\epsilon_c \sim 40\%$. At lower temperatures, dynamic recovery associated with stage III deformation in single crystals, is reduced [61] and this should result in a greater dislocation density for the same strain. The presence of the dense dislocation walls is likely a result of the greater dislocation density that is expected at cryogenic temperature. Correspondingly, more severe dislocation-based interactions take place and microstructural features develop at a greater pace than at RT.

Figure 9 shows TEM images, where microbands are identified, not just at RT, but at 77 K and 4 K as well. Microband boundaries align themselves around traces of the $\{111\}$

family of planes [50]. This is because dense dislocation walls, aligned along the $\{111\}$ trace, split up to form microbands [27, 50]. The thickness of these microbands is of the order of hundreds of nanometers ranging from ~ 200 nm at RT to ~ 450 nm at 4 K. The reason for variation in thickness is not clear and thus far literature offers no insight into any temperature/dislocation density based correlation with microband thickness. However, these widths fall in the observed range of microband widths for Al-Mg and austenitic steels [50, 62]. It is clear that despite the possible reduction of SFE with temperature in $(\text{Fe}_{40.4}\text{Ni}_{11.3}\text{Mn}_{34.8}\text{Al}_{7.5}\text{Cr}_6)\text{C}_{1.1}$, it is sufficiently high to show the formation of dense dislocation walls, linear arrays of dislocations and microbands. Correspondingly, τ_{tw} is achieved primarily through

Fig. 9 TEM-BF images of fractured specimens deformed at **a** 295 K, **c** 77 K and **d** 4 K. Corresponding TEM-DF image of **a** is shown in **b** to make it easier to identify microband. White lines indicate traces of {111} planes in **b**, **c** and **d**, placed to indicate microband walls



solid solution strengthening, where by the yield and flow stress of the material increase significantly at lower temperatures.

Thus, the interstitially alloyed ($\text{Fe}_{40.4}\text{Ni}_{11.3}\text{Mn}_{34.8}\text{Al}_{7.5}\text{Cr}_6$) $\text{C}_{1.1}$ is able to simultaneously exhibit deformation twinning and microband induced plasticity at cryogenic temperatures. It also shows a jump in σ_{YS} by a factor of ~ 3.2 , owing to high solid solution strengthening effect. This ultimately leads to achieving τ_{tw} while also retaining intermediate to HSFE deformation microstructures.

Conclusions

The present work investigates the deformation behavior of the interstitially alloyed HEA ($\text{Fe}_{40.4}\text{Ni}_{11.3}\text{Mn}_{34.8}\text{Al}_{7.5}\text{Cr}_6$) $\text{C}_{1.1}$ at cryogenic temperatures. The alloy shows multiple interesting features not seen in non-interstitial solid solutions:

1. The solid solution strengthening is very high in the present case with the σ_{YS} increasing by a factor of 3.2 as the temperature decreases from RT to 4 K.
2. The alloy shows deformation twinning at cryogenic temperatures which is likely the cause for the increased work-hardening rate at the early stages of deformation. Deformation twinning is activated at $\epsilon_t < 10\%$ at 77 and 4 K but is not observed at room temperature at any strain.
3. The alloy shows an interesting combination of both deformation twinning, characteristic of intermediate to low SFE materials, and microband formation, characteristic of intermediate to high SFE materials. The former is activated at low strains giving rise to greater work-hardening rates and the latter is activated at later stages of deformation.
4. The solute dislocation interaction leads to a significant increase in σ_{YS} sufficient for τ_{tw} to be achieved at cryogenic temperatures.
5. The present work establishes the possibility of achieving both deformation twinning and microband induced plasticity simultaneously, opening up avenues for new alloys aimed at unexplored combinations of deformation mechanisms.

Acknowledgements Financial support by the Deutsche Forschungsgemeinschaft within the framework of the Priority Program “Compositionally Complex Alloys—High-Entropy Alloys (CCA-HEA)” (SPP 2006) is gratefully acknowledged, grants no. KA 4631/1-1 and WE 6279/1-1. The authors would like to acknowledge the technical support provided by V. Tschan and S. Seils.

Author Contribution AST: Conceptualization, Methodology, Investigation, Writing—original draft, Visualization, RO: Methodology, Investigation, Writing—review & editing, IB: Resources, Methodology, Investigation, Writing—review & editing, HC: Methodology, Investigation, Writing—review & editing, K-PW: Methodology, Investigation, Writing—review & editing, MH: Resources, Writing—review & editing, Supervision, AK: Conceptualization, Methodology, Investigation, Resources, Writing—review & editing, Visualization, Supervision, Funding acquisition.

Funding Open Access funding enabled and organized by Projekt DEAL.

Data Availability The raw data required to reproduce these findings are available on request to alexander.kauffmann@kit.edu. The processed data required to reproduce these findings are available on request to alexander.kauffmann@kit.edu.

Declarations

Conflict of interest The authors declare that they have no known competing financial interests or personal relationships that could have appeared to influence the work reported in this paper.

Open Access This article is licensed under a Creative Commons Attribution 4.0 International License, which permits use, sharing, adaptation, distribution and reproduction in any medium or format, as long as you give appropriate credit to the original author(s) and the source, provide a link to the Creative Commons licence, and indicate if changes were made. The images or other third party material in this article are included in the article's Creative Commons licence, unless indicated otherwise in a credit line to the material. If material is not included in the article's Creative Commons licence and your intended use is not permitted by statutory regulation or exceeds the permitted use, you will need to obtain permission directly from the copyright holder. To view a copy of this licence, visit <http://creativecommons.org/licenses/by/4.0/>.

References

- J.W. Yeh, Physical metallurgy of high-entropy alloys. *J. Miner. Metals Mater. Soc.* **67**(10), 2254–2261 (2015)
- J.W. Yeh, Y.L. Chen, S.J. Lin, S.K. Chen, High-entropy alloys—a new era of exploitation. *Mater. Sci. Forum* **560**, 1–9 (2007)
- B.S. Murty, J.W. Yeh, S. Ranganathan, *High-Entropy Alloys* (Elsevier, Amsterdam, 2014)
- E.P. George, D. Raabe, R.O. Ritchie, High-entropy alloys. *Nat. Rev. Mater.* **4**, 515–534 (2019)
- D.B. Miracle, J.D. Miller, O.N. Senkov, C. Woodward, M.D. Uchic, J. Tiley, Exploration and development of high entropy alloys for structural applications. *Entropy* **16**, 494–525 (2014)
- D.B. Miracle, O.N. Senkov, A critical review of high entropy alloys and related concepts. *Acta Mater.* **122**, 448–511 (2017)
- Y. Zhang, T.T. Zuo, Z. Tang, M.C. Gao, K. Dahmen, P. Liaw, Z. Lu, Microstructures and properties of high-entropy alloys. *Prog. Mater. Sci.* **61**, 1–93 (2014)
- F. Otto, A. Dlouhý, C. Somsen, H. Bei, G. Eggeler, E.P. George, The influences of temperature and microstructure on the tensile properties of a CoCrFeMnNi high-entropy alloy. *Acta Mater.* **61**, 5743–5755 (2013)
- Z. Wu, H. Bei, G. M. Pharr, E. P. George, Temperature dependence of the mechanical properties of equiatomic solid solution alloys with face-centered cubic crystal structures. *Acta Mater.* **81**, 428–441 (2014)
- O.N. Senkov, J.M. Scott, S.V. Senkova, D.B. Miracle, C.F. Woodward, Microstructure and room temperature properties of a high-entropy TaNbHfZrTi alloy. *J. Alloy Compd.* **509**, 6043–6048 (2011)
- H. Chen, A. Kauffmann, S. Laube, I.-C. Choi, R. Schwaiger, Y. Huang, K. Lichtenberg, F. Müller, B. Gorr, H.-J. Christ, M. Heilmaier, Contribution of lattice distortion to solid solution strengthening in a series of refractory high entropy alloys. *Metall. Mater. Trans. A* **49**, 772–781 (2018)
- W.-Y. Ching, S. San, J. Brechtl, R. Sakidja, M. Zhang, P.K. Liaw, Fundamental electronic structure and multiatomic bonding in 13 biocompatible high-entropy alloys. *NPJ Comput. Mater.* **6**, 45 (2020)
- S.H. Shim, H. Pouraliakbar, S.I. Hong, High strength dual fcc phase CoCuFeMnNi high-entropy alloy wires with dislocation wall boundaries stabilized by phase boundaries. *Mater. Sci. Eng. A* **825**, 141875 (2021)
- A.S. Tirunilai, J. Sas, K.-P. Weiss, H. Chen, D.V. Szabó, S. Schlabach, S. Haas, D. Geissler, J. Freudenberger, M. Heilmaier, A. Kauffmann, Peculiarities of deformation of CoCrFeMnNi at cryogenic temperatures. *J. Mater. Res.* **33**(19), 3287–3300 (2018)
- G. Laplanche, A. Kostka, C. Reinhart, J. Hunfeld, G. Eggeler, E.P. George, Reasons for the superior mechanical properties of medium-entropy CrCoNi compared to high-entropy CrMnFeCoNi. *Acta Mater.* **128**, 292–303 (2017)
- A.S. Tirunilai, T. Hanemann, K.-P. Weiss, J. Freudenberger, M. Heilmaier, A. Kauffmann, Dislocation-based serrated plastic flow of high entropy alloys at cryogenic temperatures. *Acta Mater.* **200**, 980–991 (2020)
- A.S. Tirunilai, T. Hanemann, C. Reinhart, V. Tschan, K.-P. Weiss, G. Laplanche, J. Freudenberger, M. Heilmaier, A. Kauffmann, Comparison of cryogenic deformation of the concentrated solid solutions CoCrFeMnNi, CoCrNi and CoNi. *Mater. Sci. Eng. A* **783**, 139290 (2020)
- M. Naeem, H. He, F. Zhang, H. Huang, S. Harjo, T. Kawasaki, B. Wang, S. Lan, Z. Wu, F. Wang, Y. Wu, Z. Lu, Z. Zhang, C.T. Liu, X.-L. Wang, Cooperative deformation in high-entropy alloys at ultralow temperatures. *Sci. Adv.* **6**(13), eaax4002 (2020)
- G. Laplanche, A. Kostka, O.M. Horst, G. Eggeler, E.P. George, Microstructure evolution and critical stress for twinning in the CrMnFeCoNi high-entropy alloy. *Acta Mater.* **118**, 152–163 (2016)
- S. Allain, J.-P. Chateau, O. Bouaziz, S. Migot, N. Guelton, Correlations between the calculated stacking fault energy and the plasticity mechanisms in Fe–Mn–C alloys. *Mater. Sci. Eng. A* **387–389**, 158–162 (2004)
- J. Miao, C. Slone, T.M. Smith, C. Niu, H. Bei, M. Ghazisaeidi, G.M. Pharr, M.J. Mills, The evolution of the deformation substructure in a Ni-Co-Cr equiatomic solid solution alloy. *Acta Mater.* **132**, 35–48 (2017)
- Z. Li, K.G. Pradeep, Y. Deng, D. Raabe, C.C. Tasan, Metastable high-entropy dual-phase alloys overcome the strength–ductility trade-off. *Nature* **534**, 227–230 (2016)
- Z. Li, C.C. Tasan, K.G. Pradeep, Y. Deng, D. Raabe, A TRIP-assisted dual-phase high-entropy alloy: grain size and phase

- fraction effects on deformation behavior. *Acta Mater.* **131**, 323–335 (2017)
24. Z. Wang, I. Baker, Z. Cai, S. Chen, J.D. Poplawsky, W. Guo, The effect of interstitial carbon on the mechanical properties and dislocation substructure evolution in Fe_{40.4}Ni_{11.3}Mn_{34.8}Al_{7.5}Cr₆ high entropy alloys. *Acta Mater.* **120**, 228–239 (2016)
 25. Z. Wang, H. Bei, I. Baker, Microband induced plasticity and the temperature dependence of the mechanical properties of a carbon-doped FeNiMnAlCr high entropy alloy. *Mater. Charact.* **139**, 373–381 (2018)
 26. J.D. Yoo, K.-T. Park, Microband-induced plasticity in a high Mn–Al–C light steel. *Mater. Sci. Eng. A* **496**(1–2), 417–424 (2008)
 27. B. Bay, N. Hansen, D.A. Hughes, D. Kuhlmann-Wilsdorf, Overview no. 96 evolution of fcc deformation structures in polyslip. *Acta Metall. Mater.* **40**(2), 205–219 (1992)
 28. S. Huang, W. Li, S. Lu, F. Tian, J. Shen, E. Holmström, L. Vitos, Temperature dependent stacking fault energy of FeCrCoNiMn high entropy alloy. *Scripta Mater.* **108**, 44–47 (2015)
 29. L. Rémy, A. Pineau, B. Thomas, Temperature dependence of stacking fault energy in close-packed metals and alloys. *Mater. Sci. Eng.* **36**(1), 47–63 (1978)
 30. P.C.J. Gallagher, The influence of alloying, temperature, and related effects on the stacking fault energy. *Metall. Trans.* **1**, 2429–2461 (1970)
 31. L. Remy, Temperature variation of the intrinsic stacking fault energy of a high manganese austenitic steel. *Acta Metall.* **25**(2), 173–179 (1977)
 32. T.C. Tisone, The concentration and temperature dependence of the stacking fault energy in face-centered cubic Co-Fe alloys. *Acta Metall.* **21**(3), 229–236 (1973)
 33. J.B. Nelson, D.P. Riley, An experimental investigation of extrapolation methods in the derivation of accurate unit-cell dimensions of crystals. *Proc. Phys. Soc* **57**, 160–177 (1945)
 34. J. Sas, K.-P. Weiss, N. Bagrets, Cryomak - the overview of cryogenic testing facilities in Karlsruhe. *Acta Metall. Slov.* **21**(4), 330–338 (2015)
 35. Test Methods for Tension Testing of Metallic Materials. In: ASTM 03.01, ASTM International, West Conshohocken, pp. 1–29 (2016)
 36. A.S. Argon, *Strengthening Mechanisms in Crystal Plasticity* (Oxford University Press, New York, 2008)
 37. N.L. Okamoto, K. Yuge, K. Tanaka, H. Inui, E.P. George, Atomic displacement in the CrMnFeCoNi high-entropy alloy—a scaling factor to predict solid solution strengthening. *AIP Adv.* **6**, 125008 (2016)
 38. Z.S. Basinski, The instability of plastic flow of metals at very low temperatures. II. *Aust. J. Phys.* **13**(2), 354–358 (1960)
 39. T.H. Blewitt, R.R. Coltman, J.K. Redman, Low-temperature deformation of copper single crystals. *J. Appl. Phys.* **28**, 651–661 (1957)
 40. V.V. Pustovalov, Serrated deformation of metals and alloys at low temperatures (review). *Low Temp. Phys.* **34**, 683–723 (2008)
 41. M. Naeem, H. He, S. Harjo, T. Kawasaki, W. Lin, J.-J. Kai, Z. Wu, S. Lan, X.-L. Wang, Temperature-dependent hardening contributions in CrFeCoNi high-entropy alloy. *Acta Mater.* **221**, 117371 (2021)
 42. J. Brechtel, P.K. Liaw, The serrated-flow behavior in high-entropy alloys. [arXiv:2103.14504](https://arxiv.org/abs/2103.14504) [cond-mat.mtrl-sci], pp. 1–83 (2021)
 43. B. Obst, A. Nyilas, Experimental evidence on the dislocation mechanism of serrated yielding in fcc metals and alloys at low temperatures. *Mater. Sci. Eng. A* **137**, 141–151 (1991)
 44. A. Seeger, The mechanism of glide and work hardening in face-centered cubic and hexagonal-close packed metals. In: *Dislocations and Mechanical Properties of Crystals*, John Wiley & Sons, Inc., New York, pp. 243–330 (1958)
 45. S. Curtze, V.-T. Kuokkala, Dependence of tensile deformation behavior of TWIP steels on stacking fault energy, temperature and strain rate. *Acta Mater.* **58**(15), 5129–5141 (2010)
 46. R. Kalsar, P. Khandal, S. Suwas, Effects of stacking fault energy on deformation mechanisms in Al-added medium Mn TWIP steel. *Metall. Mater. Trans. A.* **50**, 3683–3696 (2019)
 47. J.-K. Kim, B.C. De Cooman, Stacking fault energy and deformation mechanisms in Fe-xMn-0.6C-yAl TWIP steel. *Mater. Sci. Eng. A* **676**, 216–231 (2016)
 48. T.S. Byun, On the stress dependence of partial dislocation separation and deformation microstructure in austenitic stainless steels. *Acta Mater.* **51**(11), 3063–3071 (2003)
 49. N. Hansen, D.J. Jensen, Development of microstructure in FCC metals during cold work. *Philos. Trans.* **357**(1756), 1447–1469 (1999)
 50. D.A. Hughes, Microstructural evolution in a non-cell forming metal: Al-Mg. *Acta Metall. Mater.* **41**(5), 1421–1430 (1993)
 51. W.M. Stobbs, C.H. Sworn, The weak beam technique as applied to the determination of the stacking-fault energy of copper. *Philos. Mag.* **24**(192), 1365–1381 (1971)
 52. D.J.H. Cockayne, M.L. Jenkins, I.L.F. Ray, The measurement of stacking-fault energies of pure face-centred cubic metals. *Philos. Mag.* **24**(192), 1383–1392 (1971)
 53. H. Saka, Experimental evidence for Suzuki segregation to the stacking fault of an extended dislocation in a Cu-Si alloy. *Philos. Mag. A* **47**(1), 131–140 (1983)
 54. T. Kamino, Y. Ueki, H. Hamajima, K. Sasaki, K. Kuroda, H. Saka, Direct evidence for Suzuki segregation obtained by high-resolution analytical electron microscopy. *Philos. Mag. Lett.* **66**(1), 27–31 (1992)
 55. U.F. Kocks, Kinetics of solution hardening. *Metall. Trans. A* **16**, 2109–2129 (1985)
 56. S.I. Hong, C. Laird, Mechanisms of slip mode modification in F.C.C. solid solutions. *Acta Metall. Mater.* **38**(8), 1581–1594 (1990)
 57. A. Vaid, D. Wei, E. Bitzek, S. Nasiri, M. Zaiser, Pinning of extended dislocations in atomically disordered crystals. [arXiv:2110.12507](https://arxiv.org/abs/2110.12507) [cond-mat.mtrl-sci], pp. 1–21 (2021)
 58. Z. Wang, I. Baker, Interstitial strengthening of a f.c.c. FeNiMnAlCr high entropy alloy. *Mater. Lett.* **180**, 153–156 (2016)
 59. C. Niu, C.R. LaRosa, J. Miao, M.J. Mills, M. Ghazisaeidi, Magnetically-driven phase transformation strengthening in high entropy alloys. *Nat. Commun.* **9**, 1363 (2018)
 60. S. Kibey, J.B. Liu, D.D. Johnson, H. Sehitoglu, Predicting twinning stress in fcc metals: linking twin-energy pathways to twin nucleation. *Acta Mater.* **55**, 6843–6851 (2007)
 61. V. Subramanya Sarma, J. Wang, W.W. Jian, A. Kauffmann, H. Conrad, J. Freudenberger, Y.T. Zhu, Role of stacking fault energy in strengthening due to cryo-deformation of FCC metals. *Mater. Sci. Eng. A* **527**, 7624–7630 (2010)
 62. I. Gutierrez-Urrutia, D. Raabe, Microbanding mechanism in an Fe–Mn–C high-Mn twinning-induced plasticity steel. *Scripta Mater.* **69**(1), 53–56 (2013)

Publisher's Note Springer Nature remains neutral with regard to jurisdictional claims in published maps and institutional affiliations.